Journal of Advanced Ceramics
2022, **11**(12): 1944–1955
https://doi.org/10.1007/s40145-022-0658-3
ISSN 2226-4108
CN 10-1154/TQ

Research Article

Layer-structured Cr/Cr_xN coating via electroplating-based nitridation achieving high deuterium resistance as the hydrogen permeation barrier

Liyu ZHENG[a], Heping LI[a,*], Jun ZHOU[a], Xinluo TIAN[a], Zhongyang ZHENG[a], Long WANG[b], Xinyun WANG[a], Youwei YAN[a]

[a]*State Key Laboratory of Materials Processing and Die & Mould Technology, International Joint Research Laboratory of Magnetic Confinement Fusion and Plasma Physics, School of Materials Science and Engineering, Huazhong University of Science and Technology, Wuhan 430074, China*
[b]*Southwestern Institute of Physics, Chengdu 610225, China*

Received: April 21, 2022; Revised: September 3, 2022; Accepted: September 6, 2022

Abstract: Hydrogen isotope permeation through structural materials is a key issue for developing nuclear fusion energy, which will cause fuel loss and radioactive pollution. Developing ceramic coatings with high thermal shock and hydrogen resistance is an effective strategy to solve this issue. In this work, a layer-structured Cr/Cr_xN coating was successfully fabricated by a facile electroplating-based nitridation technique, which is easy, facile, and applicable to coating complex-shaped substrates. The Cr/Cr_xN coating, composed of a bottom Fe/Cr interdiffusion zone, a middle Cr layer, and a top Cr_xN layer, exhibits high bonding strength, high anti-thermal-shock ability, and high deuterium permeation resistance. Its bonding strength achieves 43.6 MPa. The Cr/Cr_xN coating remains intact even after suffering 300 thermal shock cycles under a 600 ℃–water condition. Through optimizing the nitridation temperature, the Cr/Cr_xN coating achieves a deuterium permeation reduction factor (PRF) as high as 3599 at 500 ℃. Considering its scalable fabrication technique and considerable properties, the developed Cr/Cr_xN coating may serve as a novel high-performance hydrogen permeation barrier in various fields.

Keywords: hydrogen permeation; Cr_xN; Cr; electrodeposition; thermal shock resistance

1 Introduction

During the past decades, great efforts have been dedicated to the exploration of hydrogen energy as an alternative to conventional fossil fuels, which led to rapid development of hydrogen fuel cells and nuclear fusion reactors [1,2]. The nuclear fusion reactor can release huge energy by triggering a fusion reaction between hydrogen isotopes—deuterium and tritium. As deuterium is abundant in seawater, and tritium can be produced by neutron and lithium, nuclear fusion is a sustainable energy in the future. Moreover, the fusion reaction only produces helium and neutron accompanied with the energy, which is green and clean without

* Corresponding author.
E-mail: liheping@hust.edu.cn

pollution to the Earth. Therefore, nuclear fusion energy has earned worldwide concern in recent years. 321 austenitic stainless steel is a candidate as the structural material for the fusion reactor due to its outstanding mechanical properties. However, hydrogen isotopes can easily penetrate through the 321 steel, and thus cause fuel loss, radioactive pollution, and hydrogen embrittlement. Developing ceramic coatings with high thermal shock and hydrogen resistance is an effective strategy to solve this issue [3,4]. Up to now, the most effective strategy to address this issue is to deposit ceramic coatings on the steel surface as a hydrogen permeation barrier, because hydrogen isotopes permeate much slower through ceramics than metals.

References [5–8] have been conducted toward seeking suitable materials for hydrogen permeation reduction. Metal oxide coatings such as Al_2O_3 [9,10], Cr_2O_3 [11,12], Er_2O_3 [13,14], Y_2O_3 [15,16], and their composites [17,18] have been fabricated as potential hydrogen permeation barriers. Whereas, damages are easily generated in these oxide coatings during thermal cycling, because of the big difference in thermal expansion coefficient between oxides and the steel substrate, which inevitably cause the coating failing [19]. For this reason, it is essential to develop new kinds of candidate that own both outstanding anti-thermal-shock properties and high hydrogen isotope resistance. We have firstly focused on Cr_xN, a material previously used as hard coatings and decoration films for its closer thermal expansion to steels and its superior mechanical characteristics [20,21]. As reported, metallic nitrides were stable in a lithium corrosion situation from the perspective of thermodynamics. This is also beneficial to their application in nuclear fusion reactors [22]. As reported, Cr_xN coatings are usually deposited by the magnetron sputtering method, e.g., Obrosov *et al*. [23] deposited Cr_xN coatings on the Inconel 718 superalloy, and Sidelev *et al*. [24] fabricated multilayer CrN/Cr coatings on Zr alloy to improve its oxidation resistance. Shen *et al*. [25] successfully obtained Cr_xN coatings through plasma nitriding of Cr electroplated on 304 stainless steel. Compared with the metal oxides, Cr_xN is emerging as a new type of hydrogen permeation barrier with attractive performance [26–28].

In this study, we developed electrodeposition combined with nitridation to deposit Cr_xN coatings. Such a preparation technique is simple, facile, and applicable to complicated substrates with many advantages including good controllability of coating thickness, low costs, and good scalability from laboratory to industry [29]. The obtained coating consisted of a layered steel/Cr/Cr_xN structure. Its structure evolution, micromorphology, coating bonding strength, thermal shock resistance, and hydrogen and deuterium permeation reduction property were intensively investigated. The Cr_xN coating was composed of Cr_2N and CrN phases with a bonding strength of 43.6 MPa. At a 600 ℃–water thermal cycling condition, the main body of Cr/Cr_xN coating retained well even after suffering 300 thermal shock cycles. Deuterium resistance of the coated substrate was increased by 3599 times at 500 ℃, as compared with that of the bare one. The results indicate that Cr_xN may serve as a new hydrogen permeation barrier candidate with desired combination of good bonding with the substrate, high anti-thermal-shock property, and considerable hydrogen isotope resistance. These advantages provide the possibility for its usage in hydrogen-related industries.

2 Experimental

2.1 Fabrication of Cr/Cr_xN coatings

The whole procedure for fabricating a layer-structured Cr/Cr_xN coating is schematically shown in Fig. 1. Firstly, 321 austenitic stainless steel (0.07 wt% C,

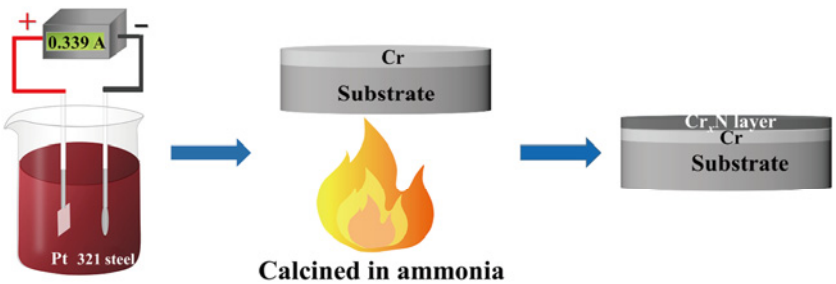

Fig. 1 Schematic diagram for fabricating a layer-structured Cr/Cr_xN coating.

18.20 wt% Cr, 10.50 wt% Ni, 1.96 wt% Mn, 0.04 wt% P, 1.00 wt% Si, and balanced Fe) was cut into wafers (ϕ20 × 0.7 mm^2), and then ground with silicon-carbide abrasives, and finally cleaned by ethyl alcohol and deionized water. Secondly, Cr electroplating was performed in aqueous solution containing 250 g/L chromic acid (CrO_3) and 2.5 g/L sulfuric acid (H_2SO_4). The optimal electroplating parameters were set according to Ref. [30], with a current density of 0.3 A/cm^2 and an electroplating time of 80 min. Thirdly, the as-deposited Cr layer was washed, dried, and calcined in ammonia at a temperature range of 650–750 ℃ for 2 h.

2. 2 Characterization

The compositions of the coatings were identified by the X-ray diffractometer (XRD, Empyrean, PANalytical B.V., the Netherlands) coupled with Cu Kα radiation (λ = 0.15406 nm) at a sweep rate of 4 (°)/min. The morphologies and microstructures of the coatings were observed by the field emission scanning electron microscope (FESEM, Nova Nano SEM 450 microscope, FEI, the Netherlands) equipped with an energy dispersive spectrometer. Further insight into the microstructure of the coatings was characterized by the transmission electron microscope (TEM, Tecnai G2 F30, FEI, the Netherlands).

The electrochemical corrosion resistance of the coatings was tested by an electrochemical workstation (CHI600E, CH Instruments, China) with a sweep rate of 50 mV/min ranged from −1 to +1 V in 3.5% NaCl solution. The bonding strength between the coating and the substrate was performed through a dual-rod pull-off method with a tensile rate of 0.5 mm/min [31]. The bonding strength was recorded from the tensile load and evaluated when the coated specimen was broken.

The deuterium permeation test at high temperatures was performed by a self-assembled system. The thermal shock resistance measurement was performed by heating the samples at 600 ℃ for 6 min, followed by quickly quenching it in water at room temperature. The thermal shock life was assessed by the number of cycles of the above steps until the coatings failed.

3 Results and discussion

3. 1 Microstructure and phase composition

The Cr_xN coating was fabricated by the nitridation of electrodeposited Cr. The Cr coating was firstly deposited on the steel surface by electroplating with optimized parameters. As shown in Fig. 2(a), there are no scratches or slag inclusions on the surface, and Cr particles arrange closely to each other, suggesting a good quality of electrodeposited Cr coating with a thickness of about 5 μm (Fig. 2(e)). The Cr coating was then converted into Cr/Cr_xN by nitridation. It is worthy to note that only the surface area of Cr was transformed to Cr_xN, and the underneath part of Cr was retained, leading to a peculiar layer-structured Cr/Cr_xN coating. The maintained Cr was speculated to be resulted from the formation of compact Cr_xN layer with small grains on the coating surfaces (Figs. 2(b) and 2(c)), which would function as a barrier to prohibit nitrogen (N) atoms from entering into the bottom of the coating [32]. The existence of Cr as a middle layer

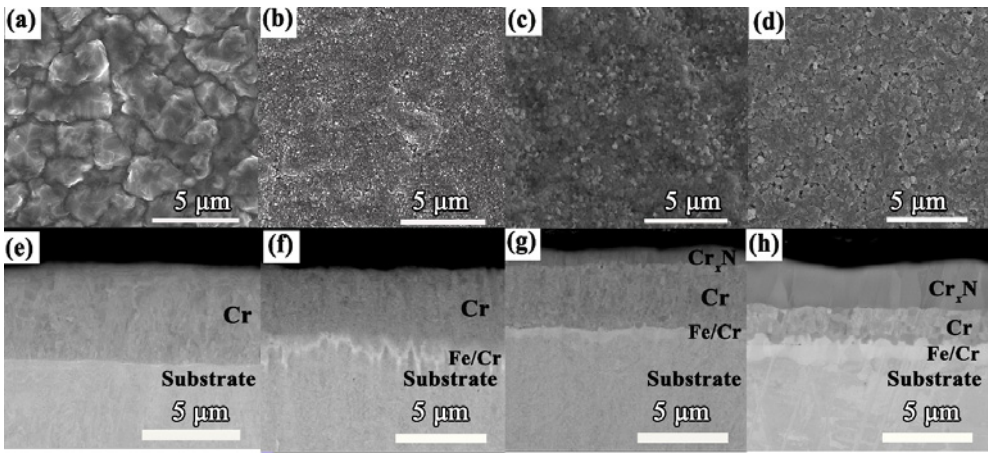

Fig. 2 Surface and cross-section back-scattered SEM images of (a, e) Cr coating and Cr/Cr_xN coatings nitrided at different temperatures: (b, f) 650 ℃, (c, g) 700 ℃, and (d, h) 750 ℃.

between the steel substrate and Cr_xN can greatly improve both the bonding strength and the thermal shock resistance (TSR) of the coating, as revealed in the later sections of bond strength test and TSR test. However, a higher nitridation temperature of 750 ℃ generated pores on the coating surface (Fig. 2(d)), probably owing to the grain growing and the CrN phase emerging. In the cross-section back-scattered electron SEM images, as shown in Figs. 2(e)–2(h), the Cr/Cr_xN was uniform and dense with no pores or cracks at the interface between Cr and Cr_xN as well as the interface between Cr and the substrate, and the Cr_xN layer became thicker with the increasing nitridation temperature. Even though micropores appear on the coating surface prepared at 750 ℃, they have not stretched through the coating, and the coating structure is dense without cracks from its cross-section SEM images. Further insight into the micromorphology of the coating was offered by the TEM images. Compared with the conventional magnetron sputtering method or arc ion plating method for obtaining metal nitrides, the electroplating-based nitridation technique is simple, facile, and convenient without requiring special and complicated apparatus [33,34]. More importantly, it is applicable to coating substrates with complex geometrical shapes.

The phase constitutions of the Cr/Cr_xN coatings nitrided at different temperatures are shown in Fig. 3(a), referred to JCPDS data for CrN (JCPDS Card No. 01-077-0047) and Cr_2N (JCPDS Card No. 00-027-0217). At 600 ℃, the presence of the diffraction peak of Cr (110) was noted intensively, suggesting an inadequate nitridation process. Compared with the JCPDS data for CrN (JCPDS Card No. 01-077-0047) and Cr_2N (JCPDS Card No. 00-027-0217), it can be seen that with the temperature increasing to above 650 ℃, strong diffraction peaks indexed to Cr_2N crystal emerged, accompanied by a set of weak peaks at 37.3°, 43.6°, and 63.1° those were ascribed to the CrN phase, indicating that Cr_2N was the dominant component at the coating surface. To be noted, a very strong (300) texture is observed in Cr_2N nitrided at 700 ℃. Similar preferred orientation of Cr_2N layers has been reported in Ref. [25]; the reason might be that the texture of the coatings is affected by the nature of different species, impinging on the growing film, the energy, and the substrate temperature [35]. However the specific mechanisms are not completely clear. A higher nitridation temperature of 750 ℃ led to a stronger diffraction peak of CrN, because the increase in ammonia dissociation and N activity at higher temperatures could generate a N-rich Cr_xN phase [36]. The elemental distributions along the depth of the coating are shown in Fig. 3(b). The Cr/Cr_xN coating nitrided at 700 ℃ consists of three parts, including a bottom Fe/Cr interdiffusion zone, a middle Cr layer of nearly 4 μm, and a top Cr_xN layer of about 2 μm. The bottom Fe/Cr interdiffusion zone could enhance the adhering strength of the coating by forming a metallurgical bonding interface, the middle Cr layer could help to remedy the thermal mismatch between the substrate and the ceramic coatings, and the top Cr_xN layer could effectively serve as a hydrogen permeation barrier. As a result, the synergistic effects of these different layers guaranteed an outstanding overall performance of such a peculiar layer-structured Cr/Cr_xN coating.

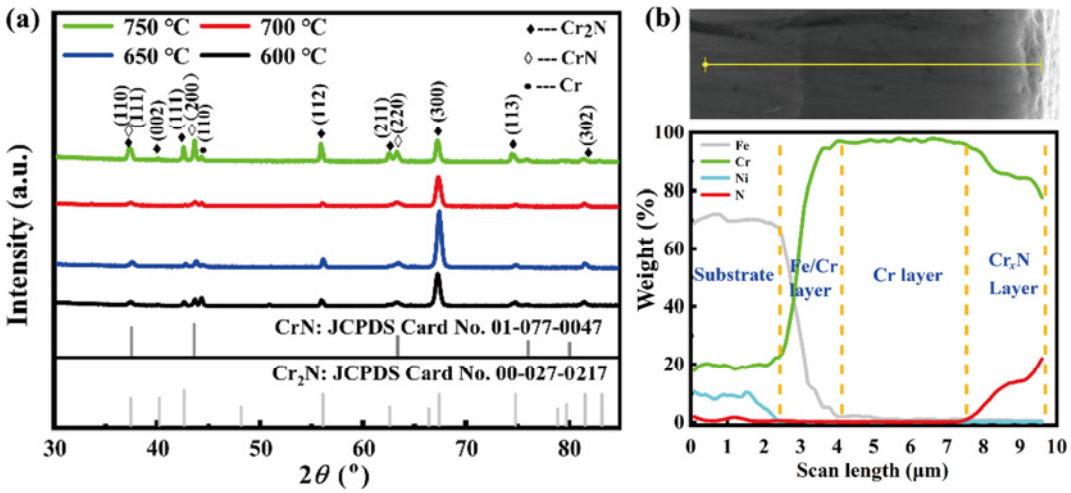

Fig. 3 (a) X-ray diffraction (XRD) patterns of Cr/Cr_xN coatings and (b) cross-section energy dispersive spectroscopy (EDS) analysis of the Cr/Cr_xN coating nitrided at 700 ℃.

Further insight into the microstructure of the Cr/Cr_xN coating nitrided at 700 ℃ was offered by the TEM images, as shown in Fig. 4. As seen, the coating was composed of nanosized little grains, whose selected area electron diffraction (SAED) pattern is shown in the inset of Fig. 4(a). The polycrystalline rings corresponding to CrN (111), Cr_2N (300), and Cr_2N (112) agreed well with the XRD results, confirming the CrN and Cr_2N components inside the coating [37,38]. The CrN nanocrystals were distributed scatteredly among the Cr_2N phase (Fig. 4(b)). In the cross-section TEM image (Fig. 4(d)), the CrN nanocrystals were also apparent on the coating surface. The interface between the middle Cr layer and the top Cr_xN layer is displayed in Fig. 4(c), and its SAED pattern shows both Cr and Cr_2N phases. At the interface, no defects such as pores or cracks were detected.

The TEM and EDS mapping images of the Cr/Cr_xN coating nitrided at 750 ℃ are shown in Fig. 5. Figure 5(a) shows the morphology of a slice cut by the focused ion beam (FIB) from cross-section of the coating; a destroyed portion next to the substrate is observed. Figure 5(b) shows a uniform polycrystalline CrN layer with a thickness of nearly 500 nm on the coating surface, and several small and isolated holes appear in this layer. In contrast, some larger holes are present in the columnar-crystallized Cr_2N layer that is underneath the CrN layer, probably caused by the hydrogen infiltration generated by ammonia decomposition during the nitridation treatment. However, these holes are discontinuous and isolated in the coating. From the high deuterium permeation resistance of the coating with the permeation reduction factor (PRF) achieving 3599, as demonstrated in the later section of deuterium permeation resistance test, this small quantity of isolated holes have not deteriorated the performance of the coating greatly. It is worthy to note that the interface between the CrN and Cr_2N layer may help to improve the deuterium resistance of the coating, and the formation of Cr and Fe/Cr layer at the bottom is favorable to enhance its bonding and anti-thermal-shock property. Figure 5(c) shows the corresponding EDS mapping image of the Cr/Cr_xN coating shown in Fig. 5(a). The N element is enriched in the surface layer and becomes less beneath the surface layer, and the Cr layer with a thickness of about 1 μm is visible. From the cross-section EDS mapping images, the absence of O element indicates that the Cr_2O_3 layer generally formed on the surface of 321 austenitic stainless steel has been eliminated during the nitridation process. It is speculated that the Cr_2O_3 film was reduced by the nascent hydrogen released from the dissociation of ammonia in the nitridation treatment [36].

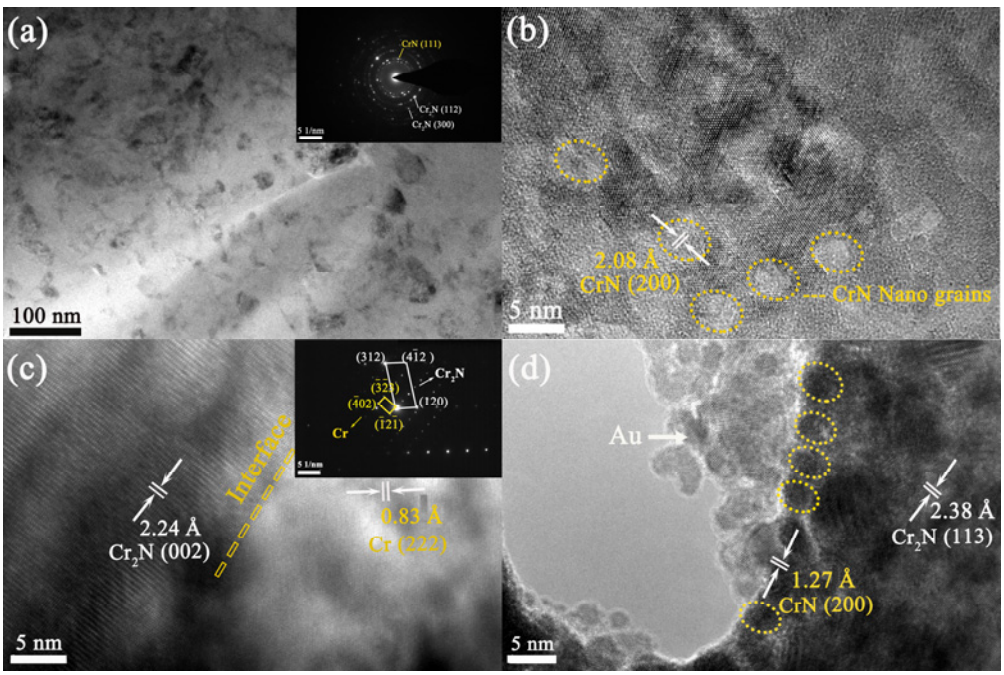

Fig. 4 TEM images of Cr/Cr_xN coating nitrided at 700 ℃: (a, b) surface areas in the coating, (c) interface between Cr_xN and Cr, and (d) outermost layer of the coating. Note: The inset in (c) is the corresponding SAED patterns.

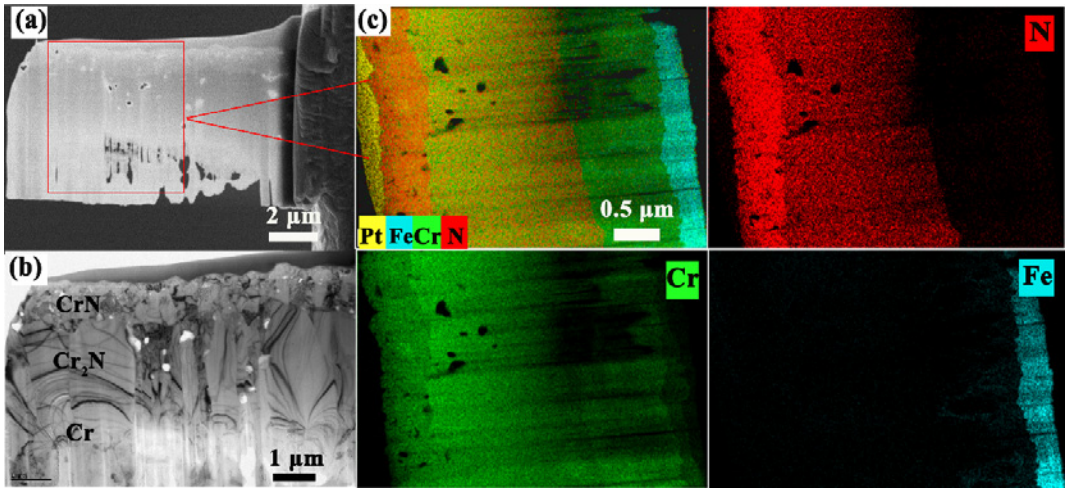

Fig. 5 Cross-section TEM images of Cr/Cr$_x$N coating nitrided at 750 ℃: (a) SEM image of a cross-section slice cut by the FIB, (b) bright-field image showing the CrN layer and Cr_2N layer, and (c) corresponding EDS mapping images of the Cr/Cr$_x$N coating shown in (a).

3. 2 Corrosion resistance and bond strength

The electrochemical corrosion resistance of the coating was tested to evaluate its compactness. The polarization curves of 321 steel and Cr/Cr$_x$N coatings are shown in Fig. 6(a). Generally, a larger positive corrosion voltage or a smaller corrosion current indicates a higher corrosion resistance [39]. Compared to that of the bare substrate, the corrosion voltage of the Cr/Cr$_x$N coating shifted 150 mV towards a positive direction, with the corrosion current density decreased by more than one order of magnitude (from 2.0×10^{-5} to 7.4×10^{-7} A/cm^2). Among these coatings, the one nitrided at 700 ℃: possessed the highest corrosion resistance, revealing the most compact structure of the coating obtained at this temperature. The bonding strengths of the coatings are shown in Fig. 6(b), which all achieved above 30 MPa, and the maximum value reached as high as 43.6 MPa. Compared with those of the previously reported metal oxide coatings [30,40], the bonding strength of the Cr/Cr$_x$N coatings is much bigger, which is attributed to the metallurgical bonding interface formed at the bottom Fe/Cr interdiffusion zone [41]. A high bonding strength can protect the coating from falling off when suffered external forces.

3. 3 Deuterium permeation resistance

The deuterium permeation resistance of the Cr/Cr$_x$N coatings nitrided at different temperatures was assessed by a deuterium gas-driven permeation device, as shown in Fig. 7(a). The deuterium permeation device consists of an upstream and downstream vacuum chamber. During the measurements, both the two chambers were pumped to achieve a low pressure around 10^{-5} Pa, and then pure hydrogen (99.9999%) was injected into the upstream until reaching a pressure of 4×10^4 Pa. Once deuterium atoms penetrated through the sample and entered the downstream vacuum chamber, their ion current could

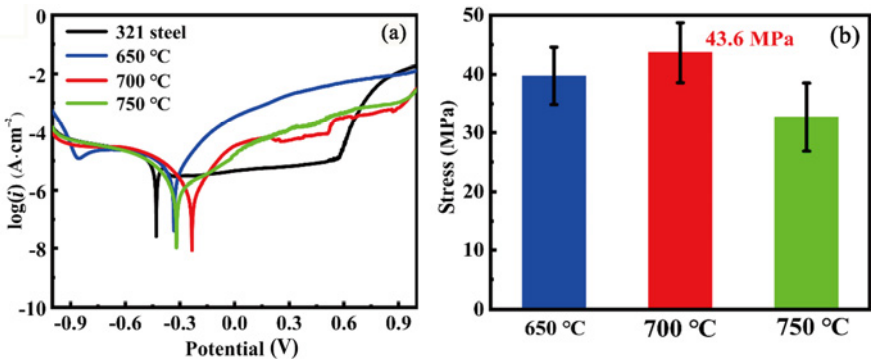

Fig. 6 (a) Corrosion resistance and (b) bonding strength of Cr/Cr$_x$N coatings.

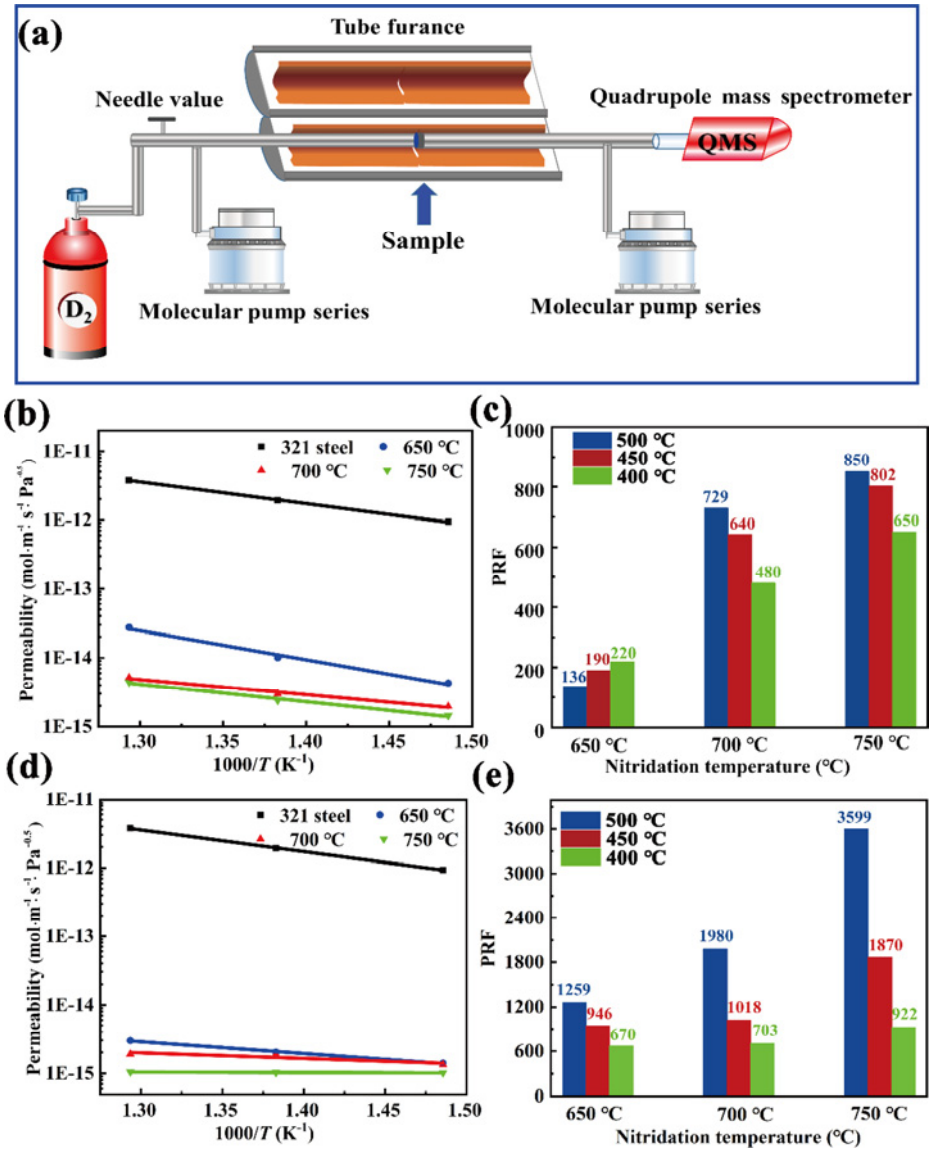

Fig. 7 (a) Home-made deuterium permeation device; deuterium permeabilities and PRFs calculated at different nitridation temperatures with different testing temperatures: (b, c) one-side-coated Cr/Cr$_x$N coatings and (d, e) double-side-coated ones.

be recorded by a quadrupole mass spectrometer (QMS, PrismaPro QMG 250 M1, Pfeiffer Vacuum, Germany). The deuterium permeation measurement can be conducted at controllable temperatures by using a furnace to heat the sample during the measuring process. During the deuterium permeation test, the number of deuterium atoms that penetrated through the sample was too small to significantly affect the deuterium pressure in the upstream, which made the pressure remain at 4×10^4 Pa until the test ended. For this reason, the deuterium permeation test was taken directly by increasing or decreasing the temperature on the basis of the former test, in agreement with the method, as reported in Refs. [42,43]. The permeation flux rate of deuterium through the sample (J) is typically expressed by the following equation: $J = P\cdot p^n/d$, where P (mol·m^{-1}·s^{-1}·Pa$^{-0.5}$) means the deuterium permeability of the sample, p (Pa) is the driving pressure, d is the sample thickness, and n indicates the pressure exponent, which is commonly regarded as 0.5 [44].

As the electroplating-based nitridation technique developed here has an inherent advantage to coating both sides of the substrate, the samples of one-side-coated substrate and double-side-coated substrate were all prepared at different nitrided temperatures for the measurement. As shown in Fig. 7(b), all the Cr/Cr$_x$N coatings nitrided at different temperatures exhibit a much lower deuterium permeability compared with

321 steel. The deuterium PRF is calculated by dividing the deuterium permeability of 321 steel by that of the coated one. The highest PRFs reach 850 and 729 for the Cr/Cr_xN coating nitrided at 750 and 700 ℃, respectively (Fig. 7(c)). It is speculated that both the phases and the coating structures have a great influence on the PRF. Generally speaking, the hydrogen isotope permeation through a coating can be depicted into two predominant processes—solution and diffusion, probably including five steps: absorbing at the surface, dissociating into atoms, dissolving into barriers, diffusing through barriers, and recombining on downsides [43,45]. Compared with the hexagonal close-packed (hcp)-Cr_2N, the face-centered cubic (fcc)-CrN with a higher packing density is more capable for preventing the penetration of deuterium atoms through the crystals in the coating [23]. And the dense nano-polycrystalline CrN formed by nitridation at 750 ℃ decreases the grain gaps and reduces the penetration channels of deuterium atoms; consequently, the coating nitrided at 750 ℃ has a relatively high PRF [26]. Furthermore, Fig. 7(c) shows a higher increase in the PRF along with the test temperature. Watching more in detail, it is worth highlighting that the deuterium permeation through the bare steel sample is negligible at lower temperatures below 400 ℃. With the increasing temperature, the deuterium flux through bare steel dramatically increases, while it is nearly a constant for the coated samples; hence, the PRF increases with the temperature. This phenomenon was also revealed in the research of Al_2O_3 coatings [42]. The double-side coating displays a far lower deuterium permeability than one-side coating (Fig. 7(d)), and the PRF of each coating is shown in Fig. 7(e). Consistent with the single-sided coating results, the double-sided coating nitrided at 750 ℃ has the best deuterium permeation resistance, and the PRF reaches 3599 at 500 ℃. This value is almost 16-30 times those of the Cr_xN coatings prepared by physical vapor deposition with the PRFs of 117–236 [27]. To be noted, the deuterium permeability of 321 steel determined in this work was in good agreement with the data obtained in Ref. [30], and thus verified the reliability of the deuterium permeation measurement. Up to date, the deuterium permeation resistance of Cr/Cr_xN coatings was almost among the highest value as reported before.

After deuterium permeation test, the surface morphologies of the Cr/Cr_xN coating nitrided at 750 ℃ are further characterized, and the SEM images are shown Fig. 8. No cracks are observed on the coating surface. For the double-side sample, the cross-section image of the coating nitrided at 700 ℃ facing the deuterium gas chamber was characterized by the TEM (Fig. 9). In Fig. 9(a), the Pt layer is deposited to form a protective layer. In the cross-section morphologies of the Cr/Cr_xN coating both before and after deuterium permeation, there were CrN crystals formed on the coating surface, which resulted in N enrichment in the surface layer; meanwhile, almost no micropores observed. As a result, defects were still visible in Cr_2N phases but not expanded, as seen in Fig. 9(a), indicating the excellent stability of the Cr/Cr_xN coatings; moreover, these defects were basically distributed at the interface between neighbouring layers. In addition, no defects were found in the middle Cr layer. The diffusion of Cr element from the coating to the substrate forming a bottom Fe/Cr interdiffusion zone was again observed in the EDS mapping images (Fig. 9(b)). As shown in Figs. 9(c) and 9(d), the crystal structures of both CrN and Cr_2N were well retained after deuterium permeation, which means that the Cr_xN phases are stable in a deuterium atmosphere.

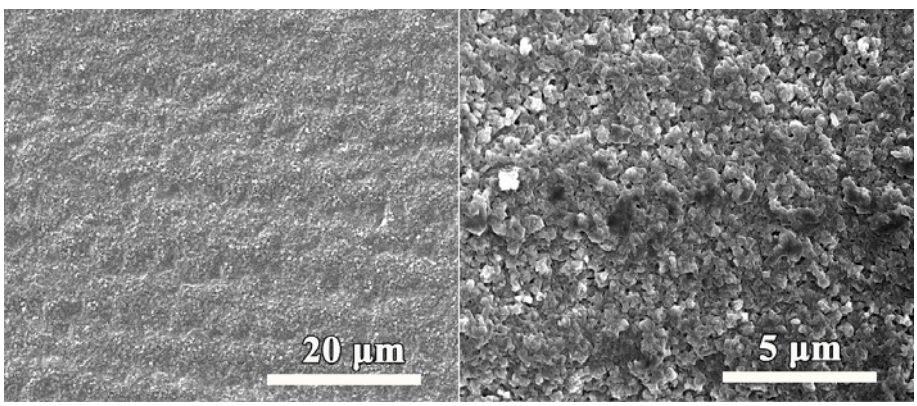

Fig. 8 Surface SEM images of Cr/Cr_xN coating nitrided at 750 ℃ after deuterium permeation test.

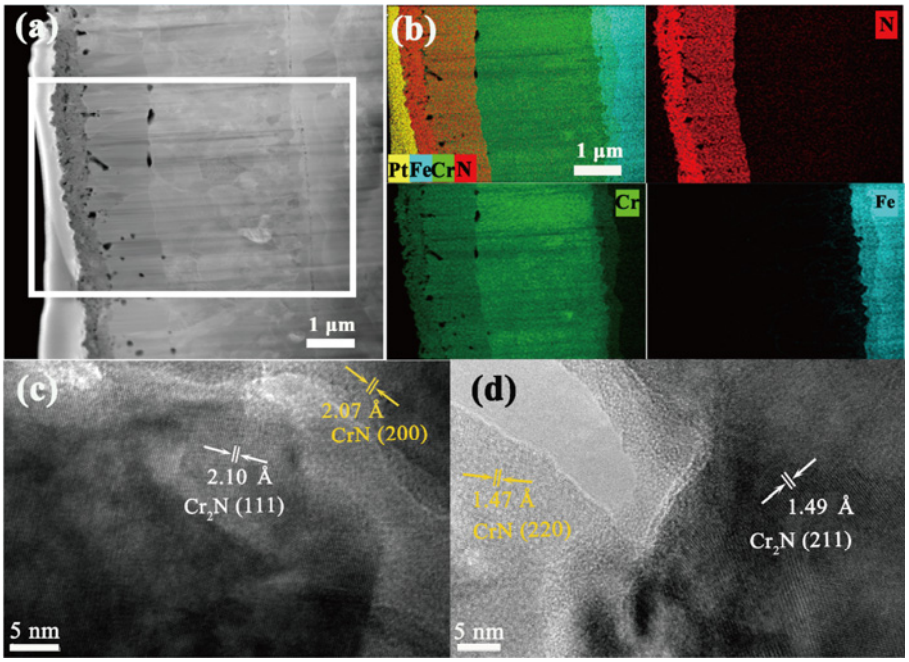

Fig. 9 (a) Cross-section TEM image and (b) EDS mapping images of Cr/Cr$_x$N coating nitrided at 700 ℃ after deuterium permeation test; (c, d) cross-section HRTEM images of Cr/Cr$_x$N coating nitrided at 700 ℃ after deuterium permeation test.

3. 4 Thermal shock resistance

TSR is another quite important property required by the hydrogen permeation barriers, because it directly determines the service life of the coating [46]. For this reason, the thermal shock cycling test was sufficiently conducted for the Cr/Cr$_x$N coating at a 600 ℃–cold water condition, and the results are shown in Fig. 10. The Cr/Cr$_x$N coating could hold its initial morphology without any cracks or falling off even after bearing 240 thermal shock cycles. When 300 thermal shock cycles were finished, a crack emerged at the coating edge, but the center of the coating without damage was still adhered firmly to the substrate. Figure 11 shows the surfaces and cross-section SEM images of the Cr/Cr$_x$N coating after 300 thermal shock cycles. It is dramatic to note that no matter on the surface or inside the coating, pores and cracks are inexistent in these areas, and additionally no defects are found at the interface between the coating and the substrate. These results indicate not only excellent bonding but also good thermal adaptation between the coating and substrate, which can be attributed to the unique Cr/Cr$_x$N layered structure with a Fe/Cr interdiffusion zone. The significant improvement in TSR achieved by Cr/Cr$_x$N coating may effectively solve the failure problem faced by traditional hydrogen permeation barriers, and enable the coating to be used in a long run.

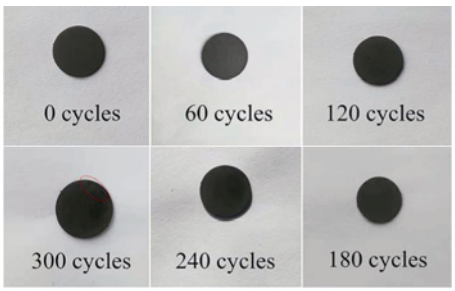

Fig. 10 Photographs of Cr/Cr$_x$N coating nitrided at 700 ℃ after different thermal shock cycles under a 600 ℃–cold water condition.

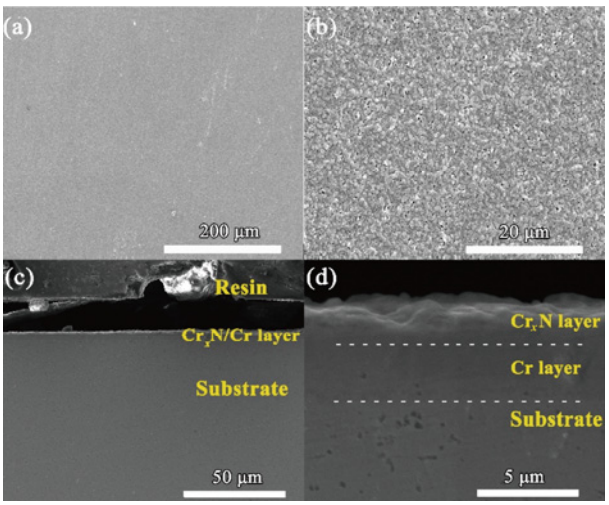

Fig. 11 SEM images of Cr/Cr$_x$N coating nitrided at 700 ℃ after 300 thermal shock cycles: (a, b) coating surface and (c, d) cross-section of the coating.

4 Conclusions

In summary, a layer-structured Cr/Cr_xN coating was successfully fabricated by a versatile electroplating-based nitridation technique, through which Cr coating was deposited on the substrate by electroplating, and then transformed into Cr/Cr_xN coating by nitridation. The Cr/Cr_xN coating was relatively compact and consisted of three parts, including a bottom Fe/Cr interdiffusion zone, a middle Cr layer, and a top Cr_xN layer. Such a unique layered structure enables the coating to own a prominent overall performance. To be specific, the bonding strength of the coating achieved up to 43.6 MPa, due to the bottom Fe/Cr interdiffusion zone that enhances the adhering strength of the coating through forming a metallurgical bonding interface. The coating could adhere firmly even after 300 thermal shock cycles at a 600 ℃–water condition, as the middle Cr layer could help to remedy the thermal mismatch between the substrate and the ceramic coatings. The deuterium PRF of the coating reached 3599 at 500 ℃, which was among the highest values as reported, suggesting that the top Cr_xN layer could effectively prevent hydrogen isotopes from permeation. Considering its facile and complex-substrate applicable fabrication method together with the marvelous combination of high bonding strength, thermal shock resistance, and hydrogen/deuterium PRF, such a peculiar layer-structured Cr/Cr_xN coating may serve as a promising and attractive barrier for hydrogen isotope permeation reduction.

Acknowledgements

This work was supported by the National MCF Energy R&D Program (Grant No. 2018YFE0313300), the National Natural Science Foundation of China (Grant No. 51402116), and the Fundamental Research Funds for the Central Universities (Grant Nos. 2018KFYYXJJ028 and 2019KFYXMBZ045). The authors thank Analytical and Testing Center of Huazhong University of Science and Technology for support.

Declaration of competing interest

The authors have no competing interests to declare that are relevant to the content of this article.

References

[1] Oshiro K, Fujimori S. Role of hydrogen-based energy carriers as an alternative option to reduce residual emissions associated with mid-century decarbonization goals. *Appl Energy* 2022, **313**: 118803.

[2] Feitosa FEB, Costa AL. Application of a multicriteria methodology for evaluation of energy alternatives for hydrogen production for the automotive sector—Case study. *Int J Hydrogen Energ* 2021, **46**: 20799–20814.

[3] Dwivedi SK, Vishwakarma M. Hydrogen embrittlement in different materials: A review. *Int J Hydrogen Energ* 2018, **43**: 21603–21616.

[4] Liu LF, Zhai CQ, Lu C, *et al*. Study of the effect of δ phase on hydrogen embrittlement of Inconel 718 by notch tensile tests. *Corros Sci* 2005, **47**: 355–367.

[5] Hollenberg GW, Simonen EP, Kalinin G, *et al*. Tritium/hydrogen barrier development. *Fusion Eng Des* 1995, **28**: 190–208.

[6] Zhang Y, Sun SK, Guo WM, *et al*. Optimal preparation of high-entropy boride–silicon carbide ceramics. *J Adv Ceram* 2021, **10**: 173–180.

[7] Lu CX, Li HP, Liu XB, *et al*. Facile fabrication and microstructure of α-Al_2O_3/TiC composite coating as tritium permeation barrier. *Int J Appl Ceram Technol* 2015, **12**: E215–E221.

[8] Li FJ, Zheng ZY, Wang XY, *et al*. Horizontally aligned BN nanosheet array for nanometer-thick ZrO_2 coating with greatly enhanced anticorrosion and hydrogen isotope resistance property. *Chem Eng J* 2022, **440**: 135920.

[9] Cao W, Ge S, Song JF, *et al*. A deuterium permeation barrier by hot-dipping aluminizing on AISI321 steel. *Int J Hydrogen Energ* 2016, **41**: 23125–23131.

[10] Zheng ZY, Li HP, Li FJ, *et al*. An efficient PDA/Al_2O_3 nanosheets reinforced ultra-thin ZrO_2 coating with attractive anti-corrosion and deuterium resistance property. *Chem Eng J* 2022, **450**: 138307.

[11] Zhou QY, Ling YH, Lu ZX, *et al*. Effect of helium implantation on the hydrogen retention of Cr_2O_3 films formed in an ultra-low oxygen environment. *Int J Hydrogen Energ* 2019, **44**: 26685–26697.

[12] Tanaka T, Chikada T, Hishinuma Y, *et al*. Formation of Cr_2O_3 layers on coolant duct materials for suppression of hydrogen permeation. *Fusion Eng Des* 2017, **124**: 1046–1051.

[13] Yang JY, Chen H, Zhang JS, *et al*. Preparation of Er_2O_3 coating on a low activation martensitic steel substrate via the route of sol–gel. *Surf Coat Technol* 2011, **205**: 5497–5501.

[14] Li Q, Wang J, Xiang QY, *et al*. Novel nano-crystalline

Er_2O_3 hydrogen isotopes permeation barriers. *J Eur Ceram Soc* 2017, **37**: 249–254.

[15] Chikada T, Matsunaga M, Horikoshi S, *et al*. Fabrication technology development and characterization of tritium permeation barriers by a liquid phase method. *Fusion Eng Des* 2018, **136**: 215–218.

[16] Engels J, Houben A, Hansen P, *et al*. Influence of the grain structure of yttria thin films on the hydrogen isotope permeation. *Int J Hydrogen Energ* 2018, **43**: 22976–22985.

[17] Sun YN, Xiang HM, Dai FZ, *et al*. Preparation and properties of CMAS resistant bixbyite structured high-entropy oxides RE_2O_3 (RE = Sm, Eu, Er, Lu, Y, and Yb): Promising environmental barrier coating materials for Al_2O_{3f}/Al_2O_3 composites. *J Adv Ceram* 2021, **10**: 596–613.

[18] Wang L, Wu YY, Luo XF, *et al*. Effects of Ar/O_2 ratio on preparation and properties of multilayer Cr_2O_3/α-Al_2O_3 tritium permeation barrier. *Surf Coat Technol* 2018, **339**: 132–138.

[19] Zhong XC, Liu F, Li XF. Transient response of a magnetoelectroelastic solid with two collinear dielectric cracks under impacts. *Int J Solids Struct* 2009, **46**: 2950–2958.

[20] Crisan O, Crisan AD. Incipient low-temperature formation of MAX phase in Cr–Al–C films. *J Adv Ceram* 2018, **7**: 143–151.

[21] Xiang HM, Xing Y, Dai FZ, *et al*. High-entropy ceramics: Present status, challenges, and a look forward. *J Adv Ceram* 2021, **10**: 385–441.

[22] Lu W, Wang J, Pu WJ, *et al*. Corrosion resistance of ceramic candidates for tritium permeation barriers exposed to molten lithium. *Corros Sci* 2019, **160**: 108172.

[23] Obrosov A, Sutygina AN, Volinsky AA, *et al*. Effect of hydrogen exposure on mechanical and tribological behavior of Cr_xN coatings deposited at different pressures on IN718. *Materials* 2017, **10**: 563.

[24] Sidelev DV, Syrtanov MS, Ruchkin SE, *et al*. Protection of Zr alloy under high-temperature air oxidation: A multilayer coating approach. *Coatings* 2021, **11**: 227.

[25] Shen HY, Wang L, Sun JC. Characteristics and properties of CrN compound layer produced by plasma nitriding of Cr-electroplated of AISI 304 stainless steel. *Surf Coat Technol* 2020, **385**: 125450.

[26] Liu LL, Ruan QD, Xiao S, *et al*. Fabrication and hydrogen permeation resistance of dense CrN coatings. *Surf Coat Technol* 2022, **437**: 128326.

[27] Matějíček J, Veverka J, Nemanič V, *et al*. Characterization of less common nitrides as potential permeation barriers. *Fusion Eng Des* 2019, **139**: 74–80.

[28] Hu LL, Wei G, Yin R, *et al*. Significant hydrogen isotopes permeation resistance via nitride nano-multilayer coating. *Int J Hydrogen Energ* 2020, **45**: 19583–19589.

[29] Wulf SE, Lorenz J, Holstein N, *et al*. Electrochemical techniques as innovative tools for fabricating divertor and blanket components in fusion technology. *Fusion Eng Des* 2019, **146**: 460–464.

[30] Wang Y, Di J, Xue LH, *et al*. Fabrication and characterization of a dense Cr_2O_3–Al phosphate double coating as tritium permeation barrier. *Fusion Eng Des* 2017, **125**: 127–133.

[31] Di J, Liu W, Xue LH, *et al*. A dense Cr_2O_3/Al_2O_3 composite ceramic coating prepared by electrodeposition and sealing with Al_2O_3. *Coatings* 2019, **9**: 14.

[32] Mayr W, Lengauer W, Ettmayer P, *et al*. Phase equilibria and multiphase reaction diffusion in the Cr–C and Cr–N systems. *J Phase Equilib* 1999, **20**: 35–44.

[33] Yang SM, Huang YT, Chang YY, *et al*. Oxidation resistance of Cr_2N and $(Cr,W)_2N$ coatings deposited on ferritic stainless steel. *Surf Coat Technol* 2017, **325**: 7–13.

[34] Guan XY, Wang YX, Xue QJ, *et al*. Toward high load bearing capacity and corrosion resistance Cr/Cr_2N nano-multilayer coatings against seawater attack. *Surf Coat Technol* 2015, **282**: 78–85.

[35] Ehrlich A, Kühn M, Richter F, *et al*. Complex characterisation of vacuum arc-deposited chromium nitride thin films. *Surf Coat Technol* 1995, **76–77**: 280–286.

[36] Ajikumar PK, Sankaran A, Kamruddin M, *et al*. Morphology and growth aspects of Cr(N) phases on gas nitridation of electroplated chromium on AISI 316 LN stainless steel. *Surf Coat Technol* 2006, **201**: 102–107.

[37] Maetz JY, Douillard T, Cazottes S, *et al*. $M_{23}C_6$ carbides and Cr_2N nitrides in aged duplex stainless steel: A SEM, TEM and FIB tomography investigation. *Micron* 2016, **84**: 43–53.

[38] Skiba O, Redjaïmia A, Dulcy J, *et al*. A proper assessment of TEM diffraction patterns originating from CrN nitrides in a ferritic matrix. *Mater Charact* 2018, **144**: 671–677.

[39] Muhammad M, Hu SH, Ma RN, *et al*. Enhancing the corrosion resistance of Q235 mild steel by incorporating poly(dopamine) modified h-BN nanosheets on zinc phosphate–silane coating. *Surf Coat Technol* 2020, **390**: 125682.

[40] Li HP, Ke ZQ, Xue LH, *et al*. A novel low-temperature approach for fabricating α-Al_2O_3-based ceramic coating as tritium permeation barrier. *Fusion Eng Des* 2017, **125**: 567–572.

[41] Zhang XM, Mu Y, Dodaran M, *et al*. Mechanical failure of CrN/Cu/CrN interfacial regions under tensile loading. *Acta Mater* 2018, **160**: 1–13.

[42] Iadicicco D, Bassini S, Vanazzi M, *et al*. Efficient hydrogen and deuterium permeation reduction in Al_2O_3 coatings

with enhanced radiation tolerance and corrosion resistance. *Nucl Fusion* 2018, **58**: 126007.

[43] Chikada T, Suzuki A, Adelhelm C, *et al*. Surface behaviour in deuterium permeation through erbium oxide coatings. *Nucl Fusion* 2011, **51**: 063023.

[44] Forcey KS, Ross DK, Simpson JCB, *et al*. Hydrogen transport and solubility in 316L and 1.4914 steels for fusion reactor applications. *J Nucl Mater* 1988, **160**: 117–124.

[45] Zhang GK, Wang XL, Xiong YF, *et al*. Mechanism for adsorption, dissociation and diffusion of hydrogen in hydrogen permeation barrier of α-Al_2O_3: A density functional theory study. *Int J Hydrogen Energ* 2013, **38**: 1157–1165.

[46] Zhao ZR, Li HP, Zheng ZY, *et al*. Improved thermal shock and corrosion resistance of α-Al_2O_3/$AlPO_4$ coating with PAA addition. *Surf Coat Technol* 2021, **414**: 127115.